Stem Cell Research & Therapy

RESEARCH

Open Access

Deficiency of extracellular vesicles miR-32 from bone marrow mesenchymal stem cells alleviates vascular calcification in type 2 diabetes by inhibiting endothelial ferroptosis

Zhengjie Lin[1†], Anqi Li[1†], Jie Zheng[1†], Kun Luo[1], Fei Liang[1], Shiyan Liu[1], Zhengfeng Liang[1], Wei Liu[1], Jian Tang[2*], Xiaolin Zhong[1,3*] and Jianghua Liu[1,3*]

Abstract

Background The development of vascular calcification (VC) in diabetes is closely related to the endothelial-to-mesenchymal transition (EndMT). We found that microRNA-32-5p (miR-32) was elevated in the plasma of calcification patients. However, it is unclear whether miR-32 mediates the function of bone marrow mesenchymal stem cell-derived extracellular vesicles (BMSC-EVs) in type 2 diabetes (T2D) VC.

Methods BMSC-EVs were characterized by TEM, NTA, Western blotting, and confocal microscopy. Alizarin Red and ALP staining assessed the severity of VC. qRT-PCR and Western blotting evaluated the expression of BMP2, RUNX2, GPX4, SLC7A11, VE-cadherin, and N-cadherin, while immunofluorescence was used for detecting VE-cadherin and N-cadherin. In vivo validation was performed using miR-32$^{-/-}$ and ApoE$^{-/-}$ mice. RNA sequencing (RNA-seq) and bioinformatics analysis was conducted to explore underlying mechanisms.

Results We demonstrated that BMSC-EVs attenuate VC in endothelial cells (ECs) and inhibit EndMT. In vivo, histological analysis showed that treatment with BMSC-EVs significantly reduced the severity of VC associated with T2D. Notably, knockout of miR-32 further enhanced the inhibitory effect of BMSC-EVs on VC. Mechanistically, transcriptomic and functional analyses suggest that the protective effect of BMSC-EVs on VC is associated with regulation of the MAPK/FoxO signaling pathway, potentially mediated by modulation of ferroptosis.

Conclusion These findings demonstrate that BMSC-EVs attenuate T2D-associated VC, partially through miR-32-mediated suppression of EC ferroptosis.

†Zhengjie Lin, Anqi Li and Jie Zheng have contributed equally to this work.

*Correspondence:
Jian Tang
tangjiancrk@163.com
Xiaolin Zhong
zhxl520@usc.edu.cn
Jianghua Liu
2018010002@usc.edu.cn

Full list of author information is available at the end of the article

Keywords Vascular calcification, Bone marrow mesenchymal stem cell-derived extracellular vesicles, microRNA-32, Ferroptosis, Endothelial-to-mesenchymal transition

Introduction

Vascular calcification (VC), characterized by abnormal mineral deposition in blood vessels, is prevalent in type 2 diabetes (T2D) patients [1, 2]. This process is considered an active and potentially modifiable physiological event. Depending on location, VC can affect the intima, media, valves, or other tissues, with T2D-associated VC primarily involving the intima and media [3, 4]. VC increases vascular stiffness and reduces compliance, leading to elevated pulse pressure, ventricular hypertrophy, altered left ventricular pressure, and changes in coronary artery diameter [5]. Studies have shown that cardiovascular disease is strongly associated with increased mortality from T2D, particularly VC [6, 7]. While some drugs and surgical interventions can mitigate VC progression, effective treatments remain lacking [8]. Addressing VC is crucial for reducing cardiovascular complications and improving T2D prognosis. Therefore, the development of novel and effective therapeutic strategies for VC is urgently needed.

Endothelial-to-mesenchymal transition (EndMT) is a hallmark of VC [9]. During EndMT, endothelial cells (ECs) begin to express markers typically associated with vascular smooth muscle cells (VSMCs) or mesenchymal stem cell-like phenotypes, such as α-SMA, SM22α, VE-cadherin, and N-cadherin [10]. This process can initially help maintain indicators of lesion stability; however, this temporary protective effect diminishes as the condition progresses to more advanced stages [11]. EndMT has also been implicated in various cardiovascular and metabolic diseases, including VC, obesity, hypertension, hyperlipidemia, and T2D. As such, it is increasingly recognized as a potential therapeutic target for vascular diseases.

The therapeutic potential of BMSCs has garnered significant attention in recent years, particularly with respect to the extracellular vesicles they secrete [12]. Bone marrow mesenchymal stem cell-derived extracellular vesicles (BMSC-EVs) are rich in bioactive substances, including proteins, RNA (miRNA, lncRNA, and mRNA), and lipids, which play vital roles in tissue repair, inflammation regulation, cellular metabolism, and various forms of cell death [13, 14]. As a novel cell-free therapeutic strategy, EVs-based therapy provides a promising alternative for injection-based treatment approaches. Accumulating evidence supports the therapeutic efficacy of BMSC-EVs in a range of disease models. For instance, BMSC-EVs have been shown to alleviate cognitive decline in Alzheimer's disease (AD)-like mice by ameliorating brain-derived neurotrophic factor (BDNF)-related neuropathology, highlighting their neuroprotective properties [15]. In musculoskeletal disorders, BMSC-EVs promoted tendon-bone healing following anterior cruciate ligament reconstruction by modulating M1/M2 macrophage polarization, thereby enhancing tissue regeneration and repair [16]. Moreover, exosomal miR-4645-5p derived from hypoxic BMSCs was found to accelerate diabetic wound healing by restoring keratinocyte autophagy, demonstrating their regulatory role in cellular stress responses and tissue repair [17]. In parallel, our previous research further revealed that plasma levels of miR-32 are significantly elevated in patients with VC compared to individuals non-VC [18]. Notably, miR-32 has been shown to regulate various biological processes in fibroblasts, VSMCs, and ECs, suggesting a potential role in the pathogenesis of vascular diseases [19]. However, the specific involvement of miR-32 in EC calcification and its underlying molecular mechanisms remain largely unexplored. Given these findings, the therapeutic potential of BMSC-EVs in T2D-associated VC, as well as their possible regulatory interaction with miR-32, warrants further investigation. However, the role and mechanisms underlying the therapeutic effects of BMSC-EVs in T2D-associated VC remain unclear.

Ferroptosis, a recently identified form of programmed cell death, is distinct from apoptosis, necrosis, and autophagy [20]. As research into ferroptosis deepens, it has been increasingly linked to a variety of diseases [21, 22]. On one hand, ferroptosis is implicated in conditions such as acute kidney disease (AKD), wound healing, osteofibrosis, and neurological disorders [23, 24]. On the other hand, ferroptosis also contributes to tumor development [25]. Recent studies have highlighted a connection between ferroptosis and VC. For instance, Hu et al. demonstrated that adrenomedullin alleviates vascular disease through the inhibition of endothelial ferroptosis [26]. Growing evidence indicates that cellular ferroptosis, particularly in VSMCs and ECs, plays a crucial role in VC progression [27, 28]. While significant advancements have been made in understanding the pathological roles of ferroptosis in various diseases, the relationship between ferroptosis and VC remains poorly understood and warrants further investigation.

This study aimed to investigate the effect of BMSC-EVs on inhibiting ferroptosis in ECs during VC associated with T2D and to elucidate the underlying mechanisms. The findings not only enhance our understanding of the mechanisms driving T2D-associated VC but also highlight the potential of BMSC-EVs as a novel preventive and therapeutic strategy for this condition.

Materials and methods

Isolation and identification of BMSCs

Four- to six-week-old wild-type male mice and miR32-deficient ApoE$^{-/-}$ mice were obtained from Vital River (Foshan, China) and maintained on a standard chow diet. To isolate BMSCs, the mice were humanely sacrificed by cervical dislocation, and bone marrow was extracted from the tibias and femurs. The bone marrow was collected in Dulbecco's modified Eagle medium (DMEM, Gibco, New York, USA). The resulting suspension was centrifuged at 1000×g for 3 min, and the pellet was resuspended in DMEM containing 10% fetal bovine serum (FBS, Gibco, New York, USA). The medium was replaced every 2–3 days.

Isolation and identification of extracellular vesicles from BMSCs

To isolate extracellular vesicles, two types of BMSCs were cultured in DMEM at 37 °C with 5% CO_2 for 48 h. To enable the accumulation of secreted extracellular vesicles, cells were cultured for 48 h in medium containing 10% EVs-depleted FBS prior to EVs isolation. The EVs isolation process began with stepwise centrifugation of the culture supernatant at 4 °C: 300 × g for 10 min, 2,000 × g for 20 min, and 10,000 × g for 30 min. The resulting supernatant was filtered through a 0.22 μm membrane and subsequently ultracentrifuged at 100,000 × g for 70 min. The pellet containing BMSC-EVs was resuspended in 100 μL of PBS. Protein concentration of BMSC-EVs was quantified using a BCA protein assay kit (Keygen, Jiangsu, China). The morphology of BMSC-EVs was examined by transmission electron microscopy (TEM; Zeiss, Germany). BMSC-EVs size distribution was measured using nanoparticle tracking analysis (NTA; Izon Science, New Zealand) based on dynamic light scattering. The expression levels of surface markers CD63 (1:1000, Abcam, UK) and CD9 (1:1000, Abcam, UK) were assessed by Western blotting. Additionally, RT-qPCR was used to determine the expression level of miR-32 in both types of BMSC-EVs.

BMSC-EVs uptake by endothelial cells (ECs)

According to the manufacturer's instructions, two types of BMSC-EVs were labeled using a DiR red fluorescent cell linker kit (Sigma, USA). Briefly, the labeling dye was added to BMSC-EVs suspended in PBS and incubated at room temperature for 10 min. The mixture was then ultracentrifuged at 100,000 × g for 70 min at 4 °C, and the labeled BMSC-EVs were resuspended in PBS. The labeled BMSC-EVs were incubated with ECs at 37 °C in 5% CO_2 for 24 h. After incubation, the cells were fixed with 4% paraformaldehyde for 15 min and washed three times with PBS. Subsequently, the nuclei were stained with DAPI (Solarbio, Beijing, China) for 10 min, followed by three additional PBS washes. Fluorescent signals were analyzed using a confocal microscope (Leica Microsystems, Germany) and ZEN 2012 imaging software.

CCK8 assay

ECs were seeded in 96-well plates at 5×10^3 cells/well and treated with BMSC-EVs (0–100 μg/ml) in EVs-depleted medium for 24 h. After treatment, 10 μL CCK-8 reagent was added to each well and incubated for 2–4 h. Absorbance was measured at 450 nm (reference 600 nm).

Measurement of EC calcification

ECs used in this study were purchased from the National Infrastructure of Cell Line Resource (China Center for Type Culture Collection) and cultured in DMEM supplemented with 10% FBS and 100 U/mL penicillin-streptomycin at 37 °C with 5% CO_2. To induce endothelial calcification, we employed a high-glucose (25 mM) basal medium supplemented with 10% FBS, 10 mM β-glycerophosphate (β-GP), and 2.5 mM calcium chloride ($CaCl_2$) as the induction system.Then ECs were co-cultured with BMSC-EVs for 14 days. In the control group, ECs were cultured in DMEM without the addition of BMSC-EVs. To assess calcification, Alizarin Red S (ARS) staining, alkaline phosphatase (ALP) staining, and calcium content measurements were performed. Specifically, Alizarin Red S staining was used to evaluate calcification. Cells were fixed in 4% paraformaldehyde for 30 min and then stained with 0.2% Alizarin Red S (Sigma, New York, USA) for 30 min. Images were captured using a microscope and analyzed using ImageJ software.

Measurement of ALP content

The level of ALP was detected using an ALP kit purchased from Biyuntian (Shanghai, China) according to the manufacturer's instructions. Briefly, cells were fixed with 4% paraformaldehyde for 15 min at room temperature, then washed with PBS. The cells were incubated with ALP staining solution according to the manufacturer's instructions at room temperature for 20–30 min in the dark. After sufficient color development, the reaction was stopped by washing with PBS, and the stained cells were observed under a light microscope.The positive staining was statistically analyzed by ImageJ software.

Measurement of calcium content

The calcium content was quantified using a calcium content kit obtained from Biyuntian (Shanghai, China) according to the manufacturer's instructions. Briefly, cells were incubated with Fluo-4 AM (5 μM) in serum-free medium at 37℃ for 30 min in the dark. After incubation, cells were washed with PBS to remove excess dye and then incubated in fresh medium for an additional 10–15 min to allow complete de-esterification.

Fluorescence was observed and captured using a fluorescence microscope. Absorbance was immediately measured at 593 nm.

Measurement of iron content

The iron content of all cells was further determined by using an iron assay kit according to the manufacturer's instructions (Dojindo, Japan). Briefly, cells were homogenized in cold iron assay buffer, and the cell extracts were collected to determine their iron contents. Absorbance was immediately measured at 593 nm.

Measurement of the ROS content

The 2'7'-dichlorofluorescein diacetate (DCFH-DA) fluorescence probe was used to detect the reactive oxygen species (ROS) accumulation in ECs. ECs were seeded into 6-well plates at a density of 2×10^5 cells per well and incubated for 24 h. Then, cells were treated with BMSC-EVs for 48 h. Cells were stained with the DCFH-DA (10 μM) fluorescence probe for 30 min at 37℃ in the dark. Cells were washed three times with serum-free cell culture medium to sufficiently remove DCFH-DA that did not enter the cells. Fluorescence intensity of DCF in different treatment groups was observed by fluorescent microscopes (Nikon, Japan) and the green fluorescence intensity was calculated by Image J.

Glutathione (GSH) and oxidized glutathione (GSSG)analysis

ECs were inoculated into 10 cm^2 dishes at a density of 5×10^6 cells/mL with 2 ml per dish. The cells were next treated with WT BMSC-EVs or miR32$^{-/-}$ BMSC-EVs. Then the cells were washed with PBS. Next, the cells were homogenized by ultrasonic crushing to obtain the cell supernatants after centrifugation. The level of GSH and GSSG (Solarbio, Beijing, China) were detected at 412 nm according to the manufactures' instructions.

Measurement of malondialdehyde (MDA)

Lipid peroxidation was assessed by measuring MDA levels using a thiobarbituric acid reactive substances (TBARS) assay kit (Biyuntian, China) according to the manufacturer's instructions. Briefly, treated cells were lysed and reacted with thiobarbituric acid (TBA) at 95 °C for 60 min. After cooling to room temperature, the absorbance of the supernatant was measured at 532 nm using a microplate reader. MDA concentrations were calculated from a standard curve generated with known MDA concentrations and normalized to the total protein content of each sample, which was determined by a BCA protein assay.

RT-qPCR

Total RNA was extracted from cells using a total RNA isolation kit (Omega, USA) according to the manufacturer's instructions. RNA was used to obtain the cDNA through reverse transcription using HiScript Reverse Transcriptase (Takara, Japan). For RT-qPCR analysis, GAPDH was used as the reference. The mRNA levels of Runx2, BMP2, OPN, GPX4, SLC7A11, ACSL4, HO-1 and VE-cadherin, N-cadherin, MMP9, Vimentin, TFRC, Nrf2 and FTH1 were analyzed using RT-qPCR and SYBR Green Supermix (Vazyme Biotech Co., Ltd.). The thermocycling conditions were: (i) Incubation step of 30 s at 90 °C; (ii) 40 cycles of 10 s at 95 °C and 30 s at 60 °C; and (iii) 15 s at 95 °C, 60 s at 60 °C and 15 s at 95 °C. The sequences of primers are listed in Table S1. All treatments and conditions were performed in triplicate and the results were calculated using the $2^{-\Delta\Delta Cq}$ method.

Western blot analysis

Total protein was extracted from cells using lysis buffer (Keygen, Jiangsu, China). The protein concentrations were determined using a BCA protein assay kit and 30 μg protein was loaded. Equal amounts of protein were separated by SDS-PAGE and transferred onto PVDF membranes, which were then blocked in 5% skim milk for 1 h at room temperature. Corresponding primary antibodies were then incubated with the membranes at 4 °C overnight. After washing, the membranes were further incubated with secondary antibodies for 1 h. ECL detection system (Nikon, Japan) was used to visualize the images, which were then evaluated. The strength of each strip was analyzed using Image J software. The primary antibodies used were as follows: Anti-GAPDH (1:1000, Abcam, UK), Anti-OPN (1:1000, Abcam, UK), Anti-Runx2 (1:1000, Abcam, UK), Anti-BMP2 (1:1000, Abcam, UK), Anti-α-SMA (1:1000, Abcam, UK), Anti-VE-cadherin (1:2000, Abcam, UK), Anti-N-cadherin (1:1000, Abcam, UK), Anti-MMP9 (1:1000, Abcam, UK), Anti-Vimentin (1:1000, Abcam, UK), Anti-GPX4 (1:1000, Abcam, UK), Anti-SLC7A11 (1:1000, Abcam, UK), Anti-ACSL4 (1:1000, Abcam, UK), Anti-HO-1 (1:1000, Abcam, UK), Anti-Nrf2 (1:1000, Abcam, UK), Anti-FTH1 (1:1000, CST, USA), and Anti-TFRC (1:1000, Abcam, UK). The secondary antibody used was Goat Anti-Rabbit IgG H&L (1:5000, Abcam, UK). The results were analyzed by image J.

Generation of T2D mice

6 weeks mice (WT and ApoE$^{-/-}$) were fed a high-fat diet (HFD) containing 10% (TP23102) or 45% (TP23100) of the energy from fat (Trophic Animal Feed High-tech Co., Ltd., Jiangsu, China) for 18 weeks. Subsequently, streptozotocin (STZ, Sigma, USA) was intraperitoneally injected at 25 mg/kg for three consecutive days. Blood glucose was monitored at specific times using a glucometer (Roche, Germany). HFD-fed mice with a blood glucose level ≥ 11.1 mM were defined as having T2D. Body weight

was measured every week for all mice. All surgical procedures were performed on animals under general anesthesia. Anesthesia was induced by placing the animals in an induction chamber and maintained via a nose cone using inhaled isoflurane (concentration: 3–4% for induction and 1.5–2% for maintenance) in a mixture of oxygen. The depth of anesthesia was monitored by assessing the absence of pedal reflexes. Following the procedures, all animals were euthanized by exposure to a rising concentration of carbon dioxide (CO2) in a controlled environment, with death confirmed by ensuring the cessation of breathing and the absence of a heartbeat.

Immunohistochemistry staining analysis

The deparaffinized sections of the aorta were prepared by heating the samples for 30 min, cooling them to room temperature, and washing them three times with 0.01 M PBS for 5 min each. Paraffin tissue samples were then sectioned to 5 μm thickness, dehydrated, treated with 3% hydrogen peroxide at room temperature for 10 min, and blocked with normal goat serum for 30 min. Next, the sections were stained with rabbit antibodies at 4℃ overnight. The following day, the sections were incubated with biotin-labeled goat anti-rabbit secondary antibody at 37℃ for 60 min and then with 50 μL streptavidin biotin peroxidase complex at room temperature for 10 min. The staining images were obtained using a microscope. The positive staining was statistically analyzed using ImageJ software.

Immunofluorescence staining analysis

To examine the expression of VE-cadherin and N-cadherin, the tissues were incubated with anti-VE-cadherin and anti-N-cadherin antibodies (1:200, Cell Signaling Technology, CST, USA) overnight at 4 °C, and then visualized with Alexa Flour 488 and 596-conjugated goat anti-rabbit antibody (1:1000, Abcam, UK). The nuclei were counterstained with DAPI (Solarbio, Beijing, China). The images were captured using a fluorescence microscope (Nikon, Japan) and analyzed with Image J software.

Alizarin red staining

Alizarin Red (Solarbio, Beijing, China) staining was used to detect ECs and arterial calcification. For cell staining, cells were fixed in paraformaldehyde for 30 min and then incubated with Alizarin Red for 30 min at room temperature. Arterial sections were stained with Alizarin Red for 30 min after fixation with 4% paraformaldehyde.

Bioinformatics analysis

Gene annotation and functional enrichment analysis were performed using the DAVID database (https://david.ncifcrf.gov/summary.jsp). Gene Ontology (GO) annotations were retrieved from the GO database (http://geneontology.org/). miRDB (https://www.mirbase.org/) was used to identify potential target genes of miR-32. Venn diagram analysis was conducted using the online tool (https://bioinfogp.cnb.csic.es/tools/venny/index.html) to identify and visualize overlapping genes.

RNA-seq analysis

Total RNA was extracted from ECtreated with β-GP + HG and BMSC-EVs miR-32$^{-/-}$, and the RNA concentration was determined using NanoDrop. Magnetic beads with oligo-dT were used to separate mRNA from total RNA, and the captured mRNA was fragmented. Finally, the sequencing library was purified using magnetic beads. After the library was constructed, the library was sequenced by PE150 using the Illumina Novaseq 6000 sequencing platform. Finally, the obtained raw sequencing sequence was subjected to bioinformatics analysis.

Statistical analysis

The results of the experiments are presented as the mean ± SD, and the analysis was performed using SPSS software (version 21.0; IBM Corp.). One-way ANOVA test was employed to evaluate the significance of differences among multiple groups. All experiments were repeated at least three times, and representative experimental data are shown in the figures. $p < 0.05$ or $p < 0.01$ were considered significant or very significant, respectively.

Statement

The work has been reported in line with the ARRIVE guidelines 2.0.

Results

BMSC-EVs from WT mice inhibited osteogenic differentiation and EndMT

BMSC-EVs were isolated from the culture media of WT BMSCs (Figure S1a). Transmission electron microscopy revealed the characteristic cup-shaped morphology of BMSC-EVs (Figure S1b). Nanoparticle tracking analysis showed that the size of BMSC-EVs was primarily distributed between 30 and 200 nm (Figure S1c). Western blot analysis confirmed high expression levels of markers CD63 and TSG101 (Figure S1d). Furthermore, uptake assays demonstrated that DiR-labeled BMSC-EVs could be internalized by ECs, as evidenced by their localization around ECs (Figure S1e), confirming effective cellular uptake.

ECs were induced by β-GP and high glucose (HG) to undergo T2D-related osteogenic differentiation in vitro for 14 days.We first employed a CCK-8 assay to assess the effects of various concentrations of BMSC-EVs on ECs. The results indicated that a concentration of 20 μg/ml did not exert any significant beneficial effect on ECs

viability (Figure S2). Consequently, this concentration was selected for use in all subsequent experiments. And then CCK-8 assay indicated that WT BMSC-EVs promoted EC proliferation (Fig. 1a). To evaluate whether WT BMSC-EVs could inhibit calcium nodule formation, Alizarin Red staining was performed, and the results demonstrated that WT BMSC-EVs significantly suppressed calcium nodule deposition compared to the β-GP group, suggesting that BMSC-EVs from WT mice effectively alleviated VC (Figs. 1b–c). Moreover, ALP staining showed that WT BMSC-EVs mitigated the activity of ALP after β-GP and HG treatment (Figs. 1d–e). Intracellular calcium quantification further revealed that WT BMSC-EVs significantly reduced calcium accumulation in ECs (Fig. 1f). Western blot analysis confirmed that WT BMSC-EVs markedly decreased the protein level of osteogenic markers BMP2, OPN, and RUNX2, with statistically significant differences (Figs. 1g–j).

Since EndMT plays a pivotal role in the pathogenesis of VC in ECs, we investigated the effect of WT BMSC-EVs on EndMT in ECs. ECs were co-cultured with WT BMSC-EVs for 48 h, during which the inhibition of EndMT was most pronounced. Western blot analysis revealed that the expression of VE-cadherin was upregulated, while the expression levels of MMP9, N-cadherin, and vimentin were significantly decreased, indicating that WT BMSC-EVs effectively suppressed EndMT in ECs (Fig. 2a and d). These findings were further validated by immunofluorescence staining, which showed increased VE-cadherin and decreased N-cadherin expression following WT BMSC-EVs treatment (Fig. 2e and h). In addition, qPCR analysis demonstrated reduced mRNA expression of EndMT-related markers, including VE-cadherin, N-cadherin, MMP9, and vimentin (Figs. 2i, S3). Taken together, these results indicate that WT BMSC-EVs inhibit EndMT and osteogenic differentiation of ECs, thereby attenuating the VC process.

BMSC-EVs from WT mice inhibited ferroptosis of ECs

In this study, we found that treatment with WT BMSC-EVs significantly reduced intracellular ROS levels (Fig. 3a and b). Quantitative iron analysis revealed that intracellular ferrous ion levels were lower in the β-GP + HG + EVs group compared to the β-GP + HG group (Fig. 3c). Given the close relationship between ferroptosis and the redox status of cells, which was reflected by GSH, GSSG, and ratio of GSH/GSSG, we examined these indicators. Our results showed that, compared to the β-GP + HG group, the β-GP + HG + EVs group exhibited increased GSH, decreased GSSG, and a reduced GSH/

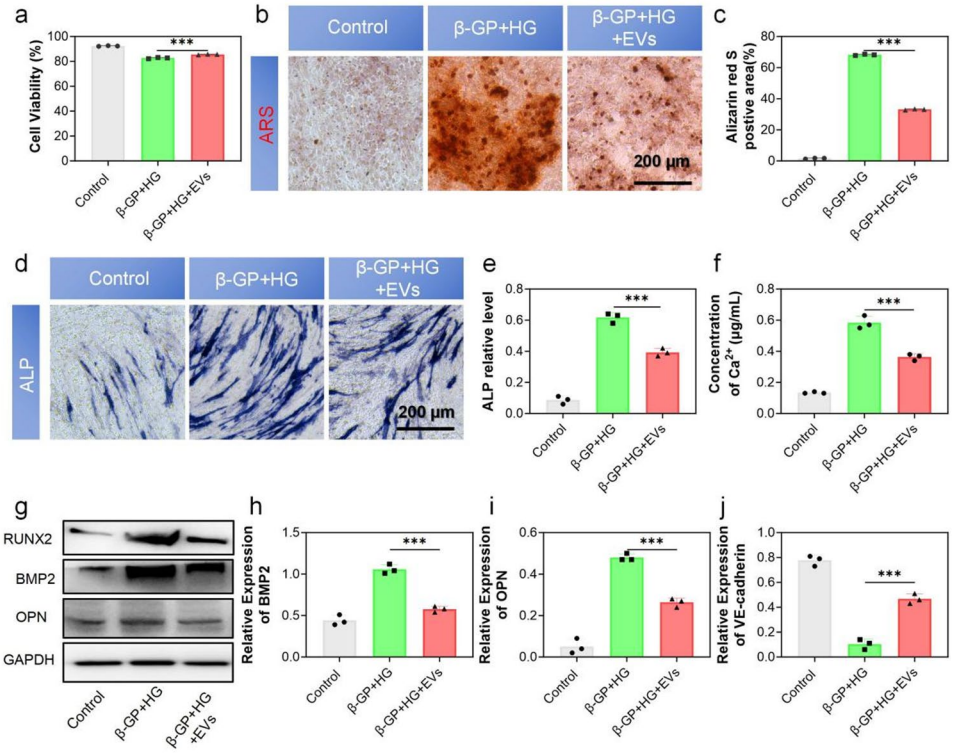

Fig. 1 BMSC-EVs attenuate VC of ECs induced by β-GP and HG. **a** Cell proliferation of ECs were assessed by CCK-8 assay following β-GP + HG or β-GP + HG + Exos treatments. **b**, **c** Calcium nodule deposition of ECs were visualized by Alizarin Red S staining with WT BMSC-EVs treatment. **d**, **e** ALP activity of ECs were measured and statistically compared. **f** Quantitative analysis of Ca^{2+} deposition of ECs across treatment groups. **g**–**j** Western blot analysis the levels of osteogenic markers (BMP2, RUNX2, and OPN). Data presented as mean ± SD. *$p < 0.05$, **$p < 0.01$, ***$p < 0.001$. $n = 3$

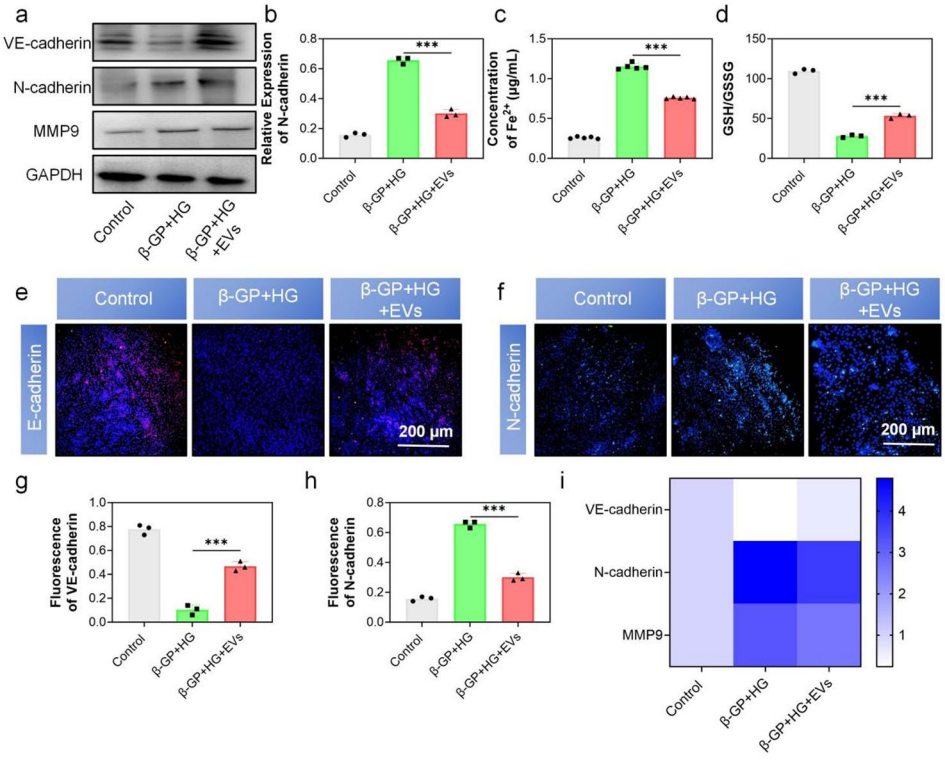

Fig. 2 WT BMSC-EVs suppress EndMT of ECs induced by β-GP and HG. **a**–**d** Western blot analysis and quantification the expression of VE-cadherin, N-cadherin and MMP9 under various treatment conditions. **e**, **f** Immunofluorescence staining analysis the expression of VE-cadherin and N-cadherin. **g**, **h** Quantitative analysis of fluorescence intensity for VE-cadherin and N-cadherin. **i** qRT-PCR analysis of VE-cadherin, N-cadherin and MMP9 expression after co-culture with BMSC-EVs. Data are presented as mean ± SD. *$p < 0.05$, **$p < 0.01$, ***$p < 0.001$. $n = 3$

GSSG ratio, suggesting effective suppression of ferroptosis (Fig. 3d and f). These findings, together with the observed reduction in intracellular peroxide production and accumulation, support the role of BMSC-EVs in mitigating oxidative stress. Furthermore, qPCR analysis showed increased mRNA expression of ferroptosis-related genes, including GPX4, SLC7A11, HO-1, Nrf2, TFRC and FTH1, following WT BMSC-EVs treatment (Fig. 3g, S4,S5f). Western blot analysis confirmed these findings at the protein level, demonstrating a significant downregulation of ACSL4 and upregulation of GPX4, SLC7A11, HO-1, Nrf2, TFRC and FTH1, (Fig. 3h and k, S5a-5d). To further verify the occurrence of ferroptosis, we measured the content of MDA, a final product of lipid peroxidation. As shown in Figure S5e, compared with the control group, the MDA levels in ECs stimulated by β-GP + HG were significantly increased, indicating strong lipid peroxidation. Importantly, treatment with BMSC-EVs can significantly reverse this elevation. Collectively, WT BMSC-EVs treatment effectively inhibited ferroptosis in ECs, reduced peroxide accumulation, and inhibited the progression of VC.

miR-32 deficiency enhances the inhibitory effect of BMSC-EVs on VC in vivo

First, WT, ApoE$^{-/-}$, and miR-32-deficiency ApoE$^{-/-}$ mice were fed a high-fat diet for 18 weeks, followed by treatment with WT BMSC-EVs three times per week for four weeks. At the end of the treatment period, the mice were sacrificed, and aortic tissues were collected for histological analysis (Fig. 4a). After 28 days of WT BMSC-EVs administration, no significant differences in body weight were observed among the groups (Fig. 4b). Alizarin Red staining revealed that, compared with WT mice, WT BMSC-EVs treatment markedly reduced aortic calcium deposition in ApoE$^{-/-}$ mice (Fig. 4c, d). In our previous studies, we demonstrated a negative correlation between miR-32 and VC in T2D [18]. Notably, WT BMSC-EVs exhibited a more pronounced inhibitory effect on vascular plaque formation in miR-32-deficient ApoE$^{-/-}$ mice. Histological examination further confirmed that WT BMSC-EVs reduced the expression of the osteogenic marker BMP2 in the vascular tissues of diabetic mice, with a markedly greater reduction observed in miR-32-deficient ApoE$^{-/-}$ mice (Fig. 4e). Immunofluorescence staining showed that WT BMSC-EVs significantly increased VE-cadherin expression while suppressing N-cadherin expression, with more prominent changes

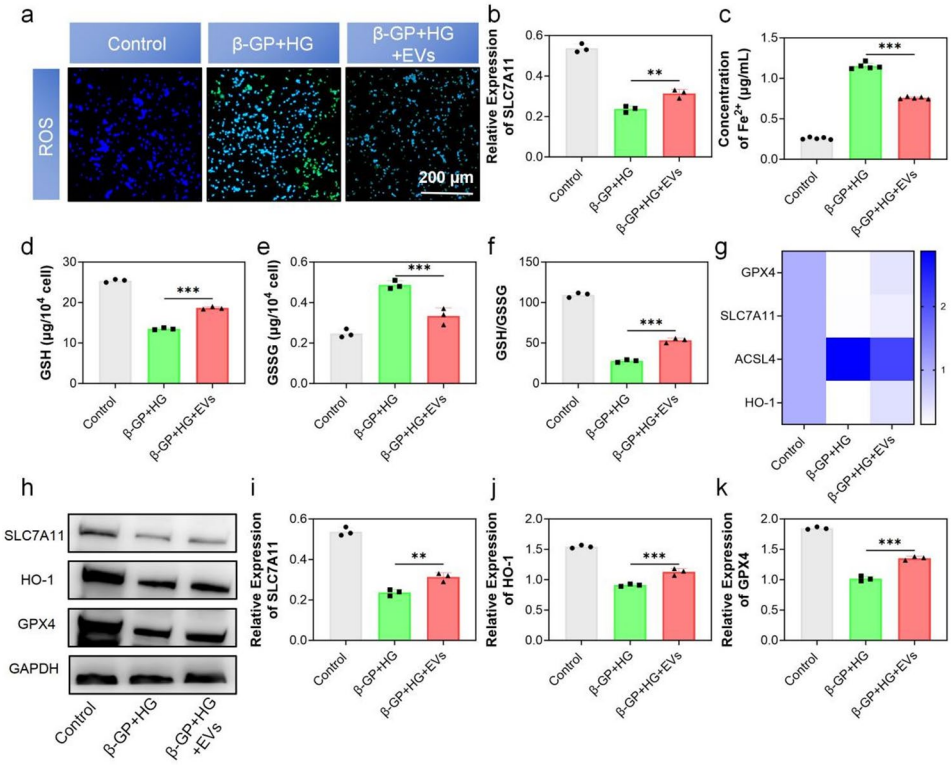

Fig. 3 WT BMSC-EVs inhibit ferroptosis of ECs induced by β-GP and HG. **a**, **b** Fluorescence staining to detect ROS levels of ECs after different treatments. **c** Assessment of the effects of WT BMSC-EVs on the expression of ferrous ions in ECs. **d**–**f** Quantify intracellular levels of GSH and GSSG, and calculate the GSH/GSSG ratio. **g** qRT-PCR was used to statistically analyze the expression of GPX4,SLC7A11,ACSL4 and HO-1. **h**–**k** Western blot statistical analysis of the expression of GPX4, SLC7A11, and HO-1 under different treatment conditions. Data are presented as mean ± SD. *$p < 0.05$, **$p < 0.01$, ***$p < 0.001$. $n = 3$

in miR-32-deficient ApoE$^{-/-}$ mice, suggesting that BMSC-EVs may inhibit EndMT and that miR-32 deletion potentiates this therapeutic effect (Fig. 4f). Additionally, immunofluorescence revealed an upregulation of GPX4 following WT BMSC-EVs treatment (Fig. 4g). BMSC-EVs administration also markedly reduced aortic calcium content in both miR-32-deficient ApoE$^{-/-}$ mice (Fig. 4h). PCR analysis further confirmed that WT BMSC-EVs significantly downregulated osteogenic differentiation–related factors, including BMP2 and RUNX2 (Figs. 4i, S6). Collectively, these findings indicate that WT BMSC-EVs attenuate vascular calcification by inhibiting osteogenic differentiation and ferroptosis, and that miR-32 deficiency enhances these protective effects.

miR32$^{-/-}$ in BMSC-EVs inhibited EC ferroptosis and osteogenic differentiation

Building on our previous work that identified miR-32 as a multifunctional regulator in cardiovascular disease [18], we further investigated its specific role in ferroptosis. To this end, we transfected endothelial cells with a miR-32 knockout construct and induced ferroptosis using a β-GP + HG stimulus. qPCR results showed that knocking out miR32 significantly reduced the mRNA content of miR32 in EC (Figure S7). Knocking out miR-32 significantly attenuated lipid peroxidation, as evidenced by reduced MDA levels (Fig. S8a). This was accompanied by decreased intracellular ferrous and calcium ion content (Figure S8b, S8c). Furthermore, miR-32 deficiency increased the GSH/GSSG ratio by elevating GSH and suppressing GSSG levels (Figure S8d-f), indicating a shift toward a more reduced redox state. Consistent with this, qPCR analysis revealed that miR-32 knockout upregulated the expression of key anti-ferroptotic genes (GPX4, SLC7A11, HO-1, Nrf2, and FTH1) while downregulating the pro-ferroptotic transporter TFRC (Figure S8g, h).

To dissect the specific contribution of miR-32 to the anti-calcific effect of BMSC-EVs, we leveraged BMSC-EVs derived from miR-32$^{-/-}$ mice as an investigative tool and assessed their impact on endothelial cell calcification. qPCR analysis confirmed that BMSC-EVs isolated from miR32-deficient mice exhibited markedly reduced miR32 levels (Figure S9).The identity of miR32$^{-/-}$ BMSC-EVs was confirmed via transmission electron microscopy, nanoparticle tracking analysis, and Western blotting. Fluorescence uptake assays demonstrated that miR-32$^{-/-}$ BMSC-EVs were efficiently internalized by ECs (Figure S1). Subsequent co-culture experiments demonstrated that treatment with miR-32–/– BMSC-EVs significantly reduced intracellular miR-32 levels in ECs (Fig. 5a and d).

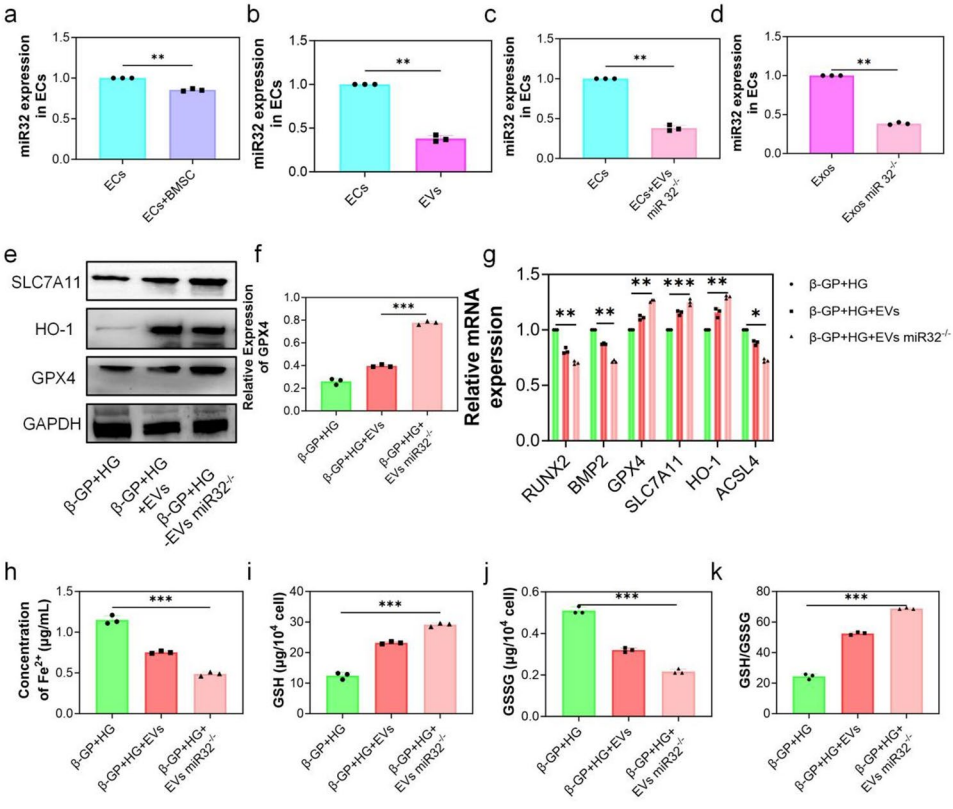

Fig. 4 miR-32 may inhibit osteogenic differentiation of ECs. **a**–**d** Expression levels of miR-32 in ECs co-cuture with BMSC, BMSC-EVs, BMSC-EVs miR32$^{-/-}$. **e**, **f** Western blot analysis of SLC7A11, GPX4 and HO-1 expression following BMSC-EVs miR-32$^{-/-}$ treatment. **g** qRT-PCR analysis of ferroptosis- and osteogenesis-related markers in ECs following treatment with Exos miR-32$^{-/-}$. **h** Assessment of the effects of BMSC-EVs miR32$^{-/-}$ on the expression of ferrous ions in ECs. **i**–**k** Quantify intracellular levels of GSH and GSSG, and calculate the GSH/GSSG ratio. Data are presented as mean ± SD. *$p < 0.05$, **$p < 0.01$, ***$p < 0.001$. $n = 3$

Notably, Western blot analysis revealed that miR-32$^{-/-}$ BMSC-EVs markedly upregulated the expression of ferroptosis-protective markers, including GPX4, SLC7A11, HO-1, Nrf2, TFRC, and FTH1 (Fig. 5e, f, S10a, S10b, S11a-S11d). Consistent with these findings, qRT-PCR results showed enhanced expression of GPX4, SLC7A11, and HO-1, alongside a significant reduction in the osteogenic markers RUNX2 and BMP2 (Fig. 5g, S11f). Moreover, miR-32$^{-/-}$ BMSC-EVs significantly decreased intracellular Fe^{2+} levels (Fig. 5h) and Ca^{2+} levels (Figure S10c), elevated GSH levels, and reduced GSSG, thereby increasing the GSH/GSSG ratio—an indicator of enhanced redox homeostasis and ferroptosis resistance (Fig. 5i and k). In addition, miR-32$^{-/-}$ BMSC-EVs reduced intracellular ROS accumulation and lowered calcium ion content in ECs (Figures S8d, S10d, S10e). Finally, Alizarin Red staining confirmed that miR-32$^{-/-}$ BMSC-EVs effectively inhibited calcium salt deposition in ECs (Figures S10f, S10g). Consistent with this, the MDA assay revealed that treatment with miR-32-deficient BMSC-EVs significantly reduced lipid peroxidation, as indicated by a lower MDA content compared to the β-GP + HG (Figure S11e). Taken together, these findings highlight the pivotal role of miR-32 in regulating ferroptosis and osteogenic differentiation in ECs. The downregulation of miR-32 via BMSC-EVs enhances antioxidant defenses, inhibits oxidative damage and calcification, and thus holds promising therapeutic potential for VC.

FoxO/MAPK is a key mediator of miR32$^{-/-}$ BMSC-EVs in regulating ferroptosis

To investigate the underlying mechanism by which miR-32 regulates ferroptosis, we performed transcriptome sequencing on ECs co-cultured with miR-32$^{-/-}$ BMSC-EVs. Among the top 30 enriched pathways, the FoxO/MAPK signaling pathway emerged as a key pathway potentially regulated by miR-32 (Figs. 6a and 7d, S7a). Bioinformatics analysis further supported the pivotal role of the FoxO pathway in ferroptosis regulation (Figs. 6e, S7b). Co-culture with miR-32$^{-/-}$ BMSC-EVs led to upregulation of FoxO expression and downregulation of MAPK expression, as confirmed by both Western blotting and qPCR analyses (Fig. 6f and h, S7c). To validate the functional role of FoxO signaling, ECs were treated with the FoxO pathway activator AS1842856. Western blot and qPCR analyses demonstrated AS1842856

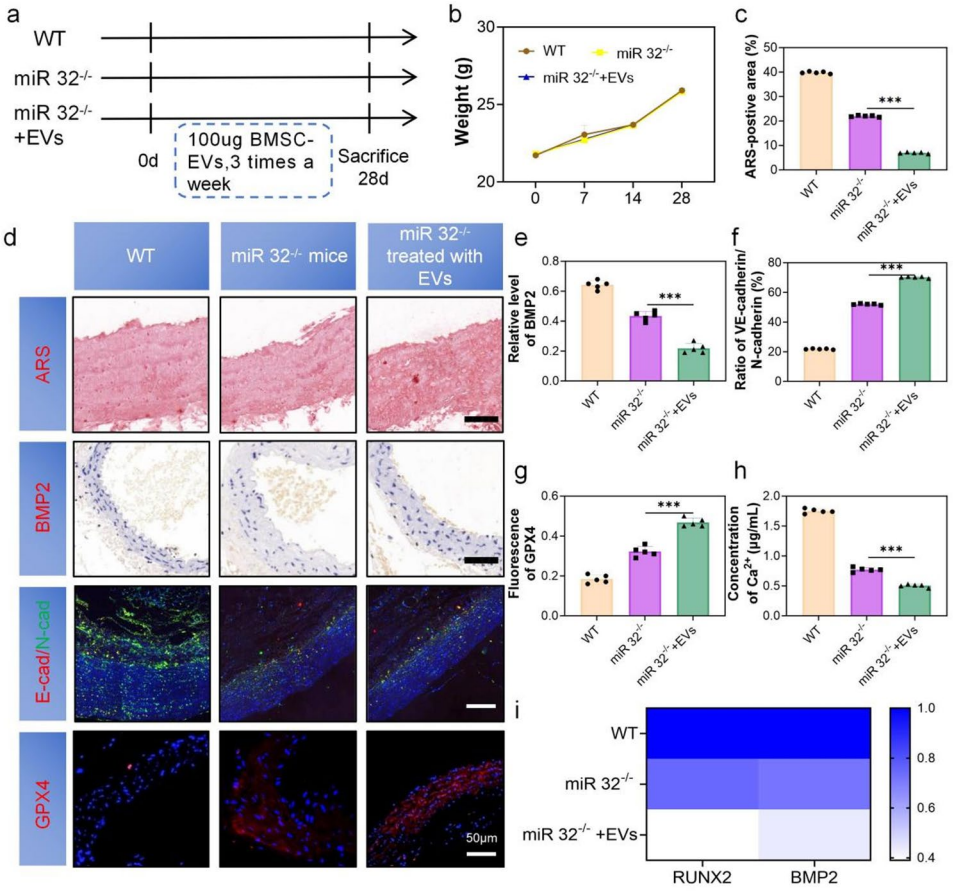

Fig. 5 Therapeutic effects of WT BMSC-EVs on VC in miR-32-deficient ApoE$^{-/-}$ mice. **a** Schematic diagram of the animal experimental design. **b** Body weight changes in mice throughout the experiment. **c** Quantitative analysis of VC of miR-32-deficient ApoE $^{-/-}$mice following BMSC-EVs treatment, assessed by Alizarin Red S (ARS) staining. **d** Evaluation of VC in miR-32-deficient ApoE$^{-/-}$ mice by ARS staining, BMP2 immunohistochemistry, and immunofluorescence staining for VE-cadherin, N-cadherin, and GPX4. **e** Quantification of BMP2 expression after BMSC-EVs treatment. **f** Quantitative analysis of the VE-cadherin/N-cadherin ratio following BMSC-EVs treatment. **g** Quantification of GPX4 expression after BMSC-EVs treatment. **h** Statistical analysis of vascular calcium content post-treatment. **i** mRNA expression levels of BMP2 and RUNX2 in vascular tissue after BMSC-EVs treatment. Data are presented as mean ± SD. *$p < 0.05$, **$p < 0.01$, ***$p < 0.001$. $n = 5$

treatment significant upregulation of ferroptosis-inhibitory markers GPX4, SLC7A11, and HO-1 (Fig. 7a and e). Moreover, AS1842856 treatment increased intracellular GSH levels while reducing GSSG levels, resulting in an elevated GSH/GSSG ratio (Fig. 7f and h). Concurrently, intracellular Fe^{2+} levels were markedly decreased (Fig. 7i), and ALP staining indicated reduced calcification activity (Figs. 7j, S7d) following AS1842856 intervention. Collectively, these findings indicate that miR-32 modulates endothelial ferroptosis and calcification, at least in part, through the FoxO/MAPK signaling axis. Enhancing FoxO signaling, either via miR-32 knockout or pharmacological activation, alleviates ferroptosis and contributes to the suppression of VC.

Discussion

Diabetes is a chronic condition characterized by impaired glucose metabolism due to pancreatic islet dysfunction [29]. VC is a chronic vascular disease which is also a common complication of diseases such as T2D and CKD. Clinical studies have shown that patients with T2D often experience intimal calcification in the arteries. Severe VC increases arterial stiffness, impairs vascular function, and can lead to vascular rupture, contributing to cardiovascular morbidity and mortality [30]. VC serves as an important pathological factor in cardiovascular disease, particularly among diabetic patients. However, finding effective strategies to inhibit VC remains a challenging issue [31]. Thus, Our findings demonstrate that BMSC-EVs alleviate T2D VC by suppressing EC ferroptosis via the FoxO/MAPK signaling pathway. Notably, the therapeutic efficacy of BMSC-EVs was further enhanced in miR-32$^{-/-}$ mice, suggesting a regulatory role of miR-32 in this process. These results are in line with previous studies and underscore the potential of BMSC-EVs as a promising miR-32-modulated therapeutic strategy for VC associated with T2D.

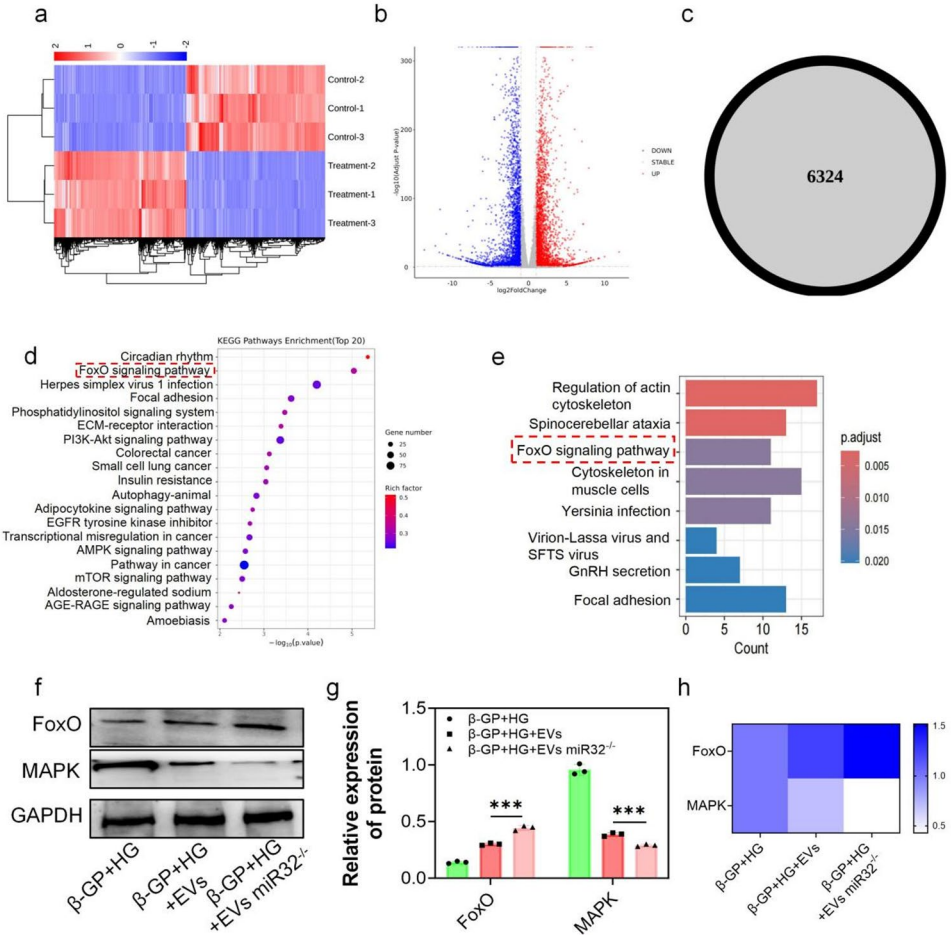

Fig. 6 miR-32 modulates endometrial cell ferroptosis via the FoxO/MAPK signaling pathway. **a**, **b** Heatmaps and volcano plots illustrating gene expression profiles in ECs between β-GP + HG and BMSC-EVs miR-32$^{-/-}$ treatment. **c** Venn diagram demonstrating differentially expressed genes between β-GP + HG and BMSC-EVs miR-32−/− groups. **d** KEGG pathway enrichment analysis of the top 30 pathways associated with the differentially expressed genes. **e** Bioinformatics analysis highlighting the top eight pathways implicated in the regulation of ferroptosis in these groups. **f**–**g** Western blot analysis showing the effect of miR-32 on the expression levels of FoxO and MAPK pathway proteins. **h** qRT-PCR was used to statistically analyze the expression of FoxO and MAPK.Data are presented as mean ± SD. *$p < 0.05$, **$p < 0.01$, ***$p < 0.001$.Data are presented as mean ± SD. *$p < 0.05$, **$p < 0.01$, ***$p < 0.001$. $n = 3$

Indeed, BMSC-EVs offer several advantages over whole cells, including a lower risk of immune response and the ability to be modified and loaded with various bioactive substances for targeted biological regulation [32, 33]. As a promising therapeutic alternative, BMSC-EVs are particularly suitable for treating complex diseases due to their reduced risk of inducing severe immune reactions compared to whole cells. Furthermore, BMSC-EVs can be engineered to carry specific molecules, allowing for more precise modulation of biological activities [34]. Interestingly, BMSC-EVs derived from macrophages containing miR-32 have been shown to play a key role in promoting arterial calcification in T2D mice by inhibiting VSMCs autophagy [31]. Although BMSC-EVs have gained increasing attention as a promising tool for stem cell-based therapy, their role in VC and the underlying mechanisms remain incompletely understood. To address this, we evaluated the therapeutic effects of BMSC-EVs derived from miR-32$^{-/-}$ mice on VC. Our results demonstrated that implantation of miR32$^{-/-}$ BMSC-EVs significantly attenuated VC in diabetic ApoE$^{-/-}$ mice, as well as in ECs subjected to β-GP and high-glucose stimulation. These findings provide compelling evidence that BMSC-EVs mitigate VC and suppress osteogenic differentiation of ECs, at least in part through miR-32-5p-mediated mechanisms. Collectively, these findings highlight the therapeutic potential of BMSC-EVs in alleviating T2D-associated VC, with notably enhanced efficacy observed upon miR-32$^{-/-}$, underscoring the critical role of miR-32 in modulating exosome-mediated vascular protection.

EndMT is a process in which ECs transform into mesenchymal-like cells, leading to the loss of endothelial function and the acquisition of osteoblast-like characteristics [35, 36]. As ECs undergo osteogenic differentiation,

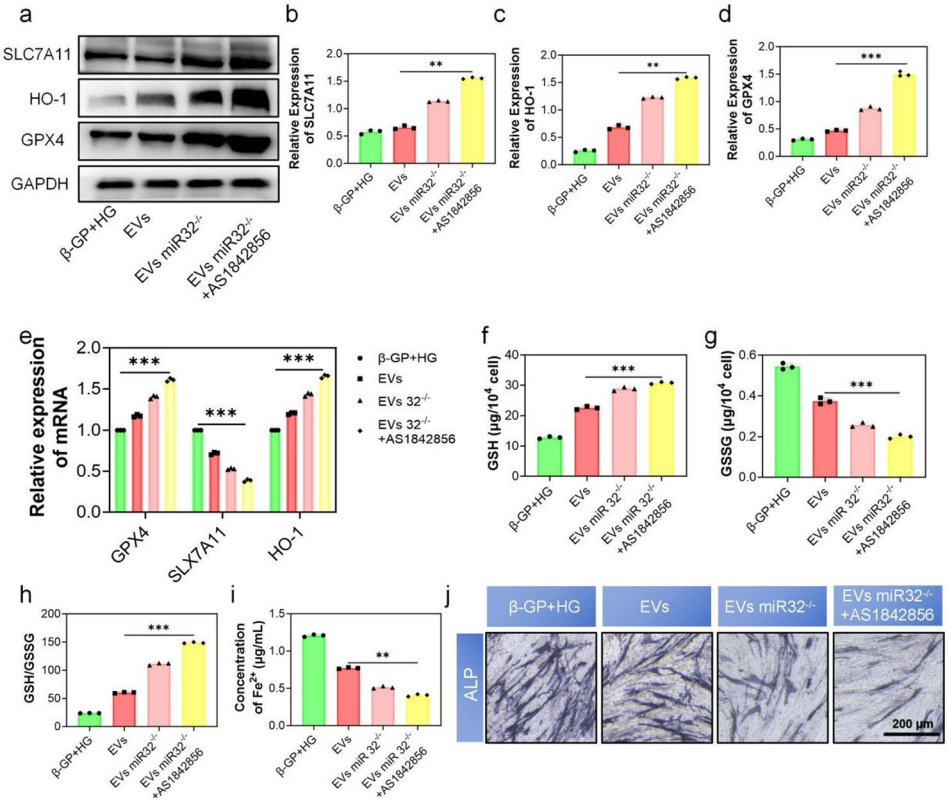

Fig. 7 Activation of the FoxO signaling pathway alleviates ferroptosis following miR-32$^{-/-}$ in ECs. **a**–**d** Western blot analysis and quantification of ferroptosis-related proteins GPX4, SLC7A11, and HO-1 under β-GP + HG, Exos, Exos miR-32$^{-/-}$, and Exos miR-32$^{-/-}$ + AS1842856 treatment conditions. **e** qPCR analysis of GPX4, SLC7A11, and HO-1 mRNA expression. **f**–**h** Quantification of intracellular GSH, GSSG, and the GSH/GSSG ratio to assess redox status under different treatments. **i** Measurement of intracellular Fe^{2+} levels. **j** ALP staining to evaluate osteogenic differentiation in ECs. Data are presented as mean ± SD. *$p < 0.05$, **$p < 0.01$, ***$p < 0.001$. $n = 3$

they secrete calcification-related proteins and minerals, ultimately contributing to VC. Previous studies have shown that BMSC-EVs can regulate osteogenic differentiation of ECs and prevent VC by carrying specific miRNAs [37]. In our study, BMSC-EVs modulated the expression of EndMT markers by delivering miR-32 to ECs. Specifically, BMSC-EVs upregulated VE-cadherin and downregulated N-cadherin expression, indicating their ability to suppress EndMT. Previous studies have demonstrated that disruption of the endothelial barrier facilitates EndMT, thereby contributing to the progression of VC and AS [38, 39]. Consistent with these findings, our results suggest that BMSC-EVs can regulate EndMT in the context of T2D-associated VC, and that miR-32$^{-/-}$ further enhances the therapeutic efficacy of BMSC-EVs.

Ferroptosis, a form of oxidative cell death, has been implicated in several diseases, including cancer, neurodegenerative disorders, and cardiovascular diseases, making it a potential therapeutic target for the treatment of these conditions [40, 41]. As mentioned previously, multiple forms of cell death have been found to play a role in the pathogenesis of VC [42–44]. Therefore, we hypothesize that preventing ferroptosis in ECs could serve as an effective strategy for vascular protection. A recent study demonstrated that inhibition of ferroptosis through the use of Fer-1 in ApoE$^{-/-}$ mice significantly attenuated VC, partially reduced iron accumulation and lipid peroxidation, and reversed the upregulation of SLC7A11 and GPX4 expression [45]. However, the role of ferroptosis in regulating T2D-related VC remains unclear. In this study, we extended these findings to ECs exposed to high glucose, as well as to rat and human arteries ex vivo and T2D VC. Our results show that elevated glucose exposure triggers ferroptosis in ECs, evidenced by increased ROS levels, elevated ACSL4 expression, reduced cell viability, and decreased levels of GSH and GPX4. Furthermore, BMSC-EVs were found to inhibit ferroptosis, leading to decreased ROS, reduced osteogenic differentiation, and significantly attenuated mineralization of ECs. In vivo, BMSC-EVs treatment also suppressed ferroptosis and improved T2D-related VC. Collectively, these findings provide strong evidence that ferroptosis acts as a positive regulator in T2D VC and highlight its potential as a therapeutic target for mitigating vascular complications in T2D.

This study has several limitations. Firstly, it relied solely on mice models, and further research is needed to determine whether BMSC-EVs can exert similar therapeutic effects in humans. Additionally, the optimal injection frequency and dosage of BMSC-EVs may vary across species, necessitating further exploration to optimize treatment protocols for future clinical applications.

Conclusion

This study successfully explores the mechanism by which BMSC-EVs influence VC. Preliminary results suggest that BMSC-EVs may inhibit VC by modulating ferroptosis. Additionally, the therapeutic effects of BMSC-EVs, particularly after the knockout of miR-32, were confirmed in vivo, demonstrating that BMSC-EVs inhibit ECs ferroptosis via the FoxO/MAPK signaling pathway to suppress VC. Therefore, BMSC-EVs regulate ferroptosis in ECs and influence EndMT, ultimately mitigating VC. This study provides a valuable foundation for further research into the mechanisms by which BMSC-EVs can be used to inhibit VC and improve our understanding of their therapeutic potential.

Abbreviations

VC	Vascular calcification
EndMT	Endothelial-to-mesenchymal transition
BMSCs	Bone marrow mesenchymal stem cells
BMSC-EVs	Bone marrow mesenchymal stem cell-derived extracellular vesicles
T2D	Type 2 diabetes
TEM	Transmission electron microscopy
NTA	Nanoparticle tracking analysis
VSMCs	Vascular smooth muscle cells
ECs	Endothelial cells
CKD	Chronic kidney disease
AKD	Acute kidney disease
ALP	Alkaline phosphatase
FBS	Fetal bovine serum
DMEM	Dulbecco's modified eagle medium
ROS	Reactive oxygen species
DCFH-DA	2'7'-dichlorofluorescein diacetate
HFD	High-fat diet
HE	Hematoxylin and eosin
ddH2O	Double-distilled water
PBS	Phosphate buffered saline
GSH	Glutathione
DAPI	4',6-diamidino-2-phenylindole
ECL	Electrochemiluminescence

Supplementary Information

The online version contains supplementary material available at https://doi.org/10.1186/s13287-026-04896-8.

Supplementary Material 1.

Supplementary Material 2.

Acknowledgements

We would like to thank Heyuan Biological Technology (Shanghai, China) for technical support in RNA sequencing analysis.

Author contributions

All authors have read and agreed to the published version of the manuscript. Z.L., A.L. and J.Z.: conceptualization, design, and execution of the experiments, methodology, data collection and analysis, manuscript preparation, and writing. K.L. F.L. and S.L.: helped with in vivo experiments, and collected data. W.L. and Z.L.: helped with animals' experiments and collection of data. J.T.： expert revision and administrative support. X.Z.: administrative support, project supervision, manuscript revision. J.L.: financial support, administrative support, and expert revision.

Funding

This work was supported by the National Natural Science Foundation of China (No.82270939 to Jianghua Liu), the Hunan Provincial Natural Science Foundation of China (2023JJ30553 to Xiaolin Zhong), and the Clinical Research 4310 Program of the First affiliated Hospital of the University of South China (20214310NHYCG02 to Jianghua Liu).

Data availability

No datasets were generated or analysed during the current study.

Declarations

Ethics approval and consent to participate

The experiment has been approved by the Animal Experimental Ethics Review Committee of the First Affiliated Hospital University of South China (Approved Project Name: Research on Type 2 Diabetes Mellitus Complicated with Coronary Artery Calcification; Ethics Reference Number: 2024LL04260001; Approval Date: April 26, 2024).

Consent for publication

Not applicable.

Competing interests

The authors declare no competing interests.

Artificial intelligence

We declared that artificial intelligence is not used in this study.

Author details

[1]Department of Endocrinology and Metabolism, The First Affiliated Hospital, Hengyang Medical School, University of South China, Hengyang 421001, Hunan, China
[2]Department of Infectious Diseases, The First Affiliated Hospital, Hengyang Medical School, University of South China, Hengyang 421001, Hunan, China
[3]Diabetes Clinical Medical Research Center of Hunan Provincial, Hengyang 421001, Hunan, China

Received: 11 August 2025 / Accepted: 2 January 2026
Published online: 10 January 2026

References

1. Pan W, Jie W, Huang H. Vascular calcification: molecular mechanisms and therapeutic interventions. MedComm (2020), 2023;4(1):e200.
2. Lee SJ, Lee IK, Jeon JH. Vascular Calcification-New insights into its mechanism. Int J Mol Sci, 2020. 21(8).
3. Sorini Dini C, Nardi G, Ristalli F, Mattesini A, Hamiti B, Di Mario C. Contemporary approach to heavily calcified coronary lesions. Interv Cardiol. 2019;14(3):154–63.
4. Yahagi K, Kolodgie FD, Lutter C, Mori H, Romero ME, Finn AV, Virmani R. Pathology of human coronary and carotid artery atherosclerosis and vascular calcification in diabetes mellitus. Arterioscler Thromb Vasc Biol. 2017;37(2):191–204.
5. Quaglino D, Boraldi F, Lofaro FD. The biology of vascular calcification. Int Rev Cell Mol Biol. 2020;354:261–353.
6. Study IH. Hypoglycaemia, cardiovascular disease, and mortality in diabetes: epidemiology, pathogenesis, and management. Lancet Diabetes Endocrinol. 2019;7(5):385–96.

7. Yun JS, Ko SH. Current trends in epidemiology of cardiovascular disease and cardiovascular risk management in type 2 diabetes. Metabolism. 2021;123:154838.
8. Cozzolino M, Maffei Faccioli F, Cara A, Boni Brivio G, Rivela F, Ciceri P, Magagnoli L, Galassi A, Barbuto S, Speciale S, Minicucci C, Cianciolo G. Future treatment of vascular calcification in chronic kidney disease. Expert Opin Pharmacother. 2023;24(18):2041–57.
9. Lu D, Jiang H, Zou T, Jia Y, Zhao Y, Wang Z. Endothelial-to-mesenchymal transition: new insights into vascular calcification. Biochem Pharmacol. 2023;213:115579.
10. Souilhol C, Harmsen MC, Evans PC, Krenning G. Endothelial-mesenchymal transition in atherosclerosis. Cardiovasc Res. 2018;114(4):565–77.
11. Newman AAC, Serbulea V, Baylis RA, Shankman LS, Bradley X, Alencar GF, Owsiany K, Deaton RA, Karnewar S, Shamsuzzaman S, Salamon A, Reddy MS, Guo L, Finn A, Virmani R, Cherepanova OA, Owens GK. Multiple cell types contribute to the atherosclerotic lesion fibrous cap by PDGFRbeta and bioenergetic mechanisms. Nat Metab. 2021;3(2):166–81.
12. Mondal J, Pillarisetti S, Junnuthula V, Saha M, Hwang SR, Park IK, Lee YK. Hybrid exosomes, exosome-like nanovesicles and engineered exosomes for therapeutic applications. J Control Release. 2023;353:1127–49.
13. Huang Y, He B, Wang L, Yuan B, Shu H, Zhang F, Sun L. Bone marrow mesenchymal stem cell-derived exosomes promote rotator cuff tendon-bone healing by promoting angiogenesis and regulating M1 macrophages in rats. Stem Cell Res Ther. 2020;11(1):496.
14. Li H, Lin W, Zhang G, Liu R, Qu M, Zhang J, Xing X. BMSC-exosomes miR-25-3p regulates the p53 signaling pathway through PTEN to inhibit cell apoptosis and ameliorate liver ischemia–reperfusion injury. Stem Cell Rev Rep, 2023;19(8):2820–2836.
15. Liu S, Fan M, Xu JX, Yang LJ, Qi CC, Xia QR, Ge JF. Exosomes derived from bone-marrow mesenchymal stem cells alleviate cognitive decline in AD-like mice by improving BDNF-related neuropathology. J Neuroinflammation. 2022;19(1):35.
16. Li Z, Li Q, Tong K, Zhu J, Wang H, Chen B, Chen L. BMSC-derived exosomes promote tendon-bone healing after anterior cruciate ligament reconstruction by regulating M1/M2 macrophage polarization in rats. Stem Cell Res Ther. 2022;13(1):295.
17. Shi Y, Wang S, Liu D, Wang Z, Zhu Y, Li J, Xu K, Li F, Wen H, Yang R. Exosomal miR-4645-5p from hypoxic bone marrow mesenchymal stem cells facilitates diabetic wound healing by restoring keratinocyte autophagy. Burns Trauma 2024;12:tkad058.
18. Liu J, Xiao X, Shen Y, Chen L, Xu C, Zhao H, Wu Y, Zhang Q, Zhong J, Tang Z, Liu C, Zhao Q, Zheng Y, Cao R, Zu X. MicroRNA-32 promotes calcification in vascular smooth muscle cells: implications as a novel marker for coronary artery calcification. PLoS ONE. 2017;12(3):e0174138.
19. Li Q, Li Z, Lin Y, Che H, Hu Y, Kang X, Zhang Y, Wang L, Zhang Y. High glucose promotes hepatic fibrosis via miR–32/MTA3–mediated epithelial–to–mesenchymal transition. Mol Med Rep. 2019;19(4):3190–200.
20. Li J, Cao F, Yin HL, Huang ZJ, Lin ZT, Mao N, Sun B, Wang G. Ferroptosis: past, present and future. Cell Death Dis. 2020;11(2):88.
21. Drueke TB, Massy ZA. Vascular calcification in chronic kidney disease: contribution of ferroptosis? Kidney Int. 2022;102(6):1209–11.
22. Ye Y, Chen A, Li L, Liang Q, Wang S, Dong Q, Fu M, Lan Z, Li Y, Liu X, Ou JS, Lu L, Yan J. Repression of the antiporter SLC7A11/glutathione/glutathione peroxidase 4 axis drives ferroptosis of vascular smooth muscle cells to facilitate vascular calcification. Kidney Int, 2022;102(6):1259–1275.
23. Chen J, Li X, Liu H, Zhong D, Yin K, Li Y, Zhu L, Xu C, Li M, Wang C. Bone marrow stromal cell-derived Exosomal circular RNA improves diabetic foot ulcer wound healing by activating the nuclear factor erythroid 2-related factor 2 pathway and inhibiting ferroptosis. Diabet Med. 2023;40(7):e15031.
24. Li J, Jia B, Cheng Y, Song Y, Li Q, Luo C. Targeting molecular mediators of ferroptosis and oxidative stress for neurological disorders. Oxid Med Cell Longev. 2022;2022:p3999083.
25. Li H, Sun Y, Yao Y, Ke S, Zhang N, Xiong W, Shi J, He C, Xiao X, Yu H, Dai P, Xiang B, Xing X, Xu G, Song W, Song J, Zhang J. USP8-governed GPX4 homeostasis orchestrates ferroptosis and cancer immunotherapy. Proc Natl Acad Sci U S A. 2024;121(16):e2315541121.
26. Hu Y, Gu X, Zhang Y, Ma W, Sun L, Wang C, Ren B. Adrenomedullin, transcriptionally regulated by vitamin D receptors, alleviates atherosclerosis in mice through suppressing AMPK-mediated endothelial ferroptosis. Environ Toxicol. 2024;39(1):199–211.
27. Bai T, Li M, Liu Y, Qiao Z, Wang Z. Inhibition of ferroptosis alleviates atherosclerosis through attenuating lipid peroxidation and endothelial dysfunction in mouse aortic endothelial cell. Free Radic Biol Med. 2020;160:92–102.
28. You J, Ouyang S, Xie Z, Zhi C, Yu J, Tan X, Li P, Lin X, Ma W, Liu Z, Hou Q, Xie N, Peng T, Chen X, Li L, Xie W. The suppression of hyperlipid diet-induced ferroptosis of vascular smooth muscle cells protests against atherosclerosis independent of p53/SCL7A11/GPX4 axis. J Cell Physiol. 2023;238(8):1891–908.
29. Tinajero MG, Malik VS. An update on the epidemiology of type 2 diabetes: A global perspective. Endocrinol Metab Clin North Am. 2021;50(3):337–55.
30. Choi Y, Yoosun Cho YCMD, Kang J, Hyun-Suk Jung ;SarahH, Wild, ; Christopher D, Byrne, editors. MBBCh; and Seungho Ryu, Prediabetes diagnosis is associated with the progression of coronary artery calcification: the Kangbuk Samsung Health Study. Diabetes Obes Metab. 2022;24(11):2118–2126.
31. Cao J, Chen C, Chen Q, Gao Y, Zhao Z, Yuan Q, Li A, Yang S, He Y, Zu X, Liu J. Extracellular vesicle miR-32 derived from macrophage promotes arterial calcification in mice with type 2 diabetes via inhibiting VSMC autophagy. J Transl Med. 2022;20(1):307.
32. Yingjie Liu SB, Guo W, Liu W. Bone mesenchymal stem cell derived exosomes alleviate high phosphorus-induced calcification of vascular smooth muscle cells through the NONHSAT 084969.2/NF-κB axis. Aging, 2021. 13(12).
33. Zeng ZL, Zhu Q, Zhao Z, Zu X, Liu J. Magic and mystery of microRNA-32. J Cell Mol Med. 2021;25(18):8588–601.
34. Li Z, Liu C, Li S, Li T, Li Y, Wang N, Bao X, Xue P, Liu S. BMSC-Derived exosomes inhibit Dexamethasone-Induced muscle atrophy via the miR-486-5p/FoxO1 axis. Front Endocrinol (Lausanne). 2021;12:681267.
35. Manfioletti G, Fedele M. Epithelial-Mesenchymal transition (EMT) 2021. Int J Mol Sci, 2022;23(10).
36. Bischoff J. Endothelial-to-Mesenchymal transition. Circ Res. 2019;124(8):1163–5.
37. Ryu J, Ahn Y, Kook H, Kim YK. The roles of non-coding RNAs in vascular calcification and opportunities as therapeutic targets. Pharmacol Ther. 2021;218:107675.
38. Ciceri P, Artioli L, Molinaro M, Falleni M, Tosi D, Martinelli C, Santo N, Rondinone O, Miozzo M, Bianchi P, Gianelli U, Fontana L, Cozzolino M. High-phosphate causes endothelial extracellular matrix calcification by inducing endothelial cell mesenchymal transition and osteoblastic differentiation. Am J Physiol Ren Physiol. 2025;328(6):F861–75.
39. Liang G, Wang S, Shao J, Jin YJ, Xu L, Yan Y, Gunther S, Wang L, Offermanns S. Tenascin-X mediates Flow-Induced suppression of EndMT and atherosclerosis. Circ Res. 2022;130(11):1647–59.
40. Zhao L, Zhou X, Xie F, Zhang L, Yan H, Huang J, Zhang C, Zhou F, Chen J, Zhang L. Ferroptosis in cancer and cancer immunotherapy. Cancer Commun (Lond). 2022;42(2):88–116.
41. Chen Y, Li X, Wang S, Miao R, Zhong J. Targeting iron metabolism and ferroptosis as novel therapeutic approaches in cardiovascular diseases. Nutrients, 2023. 15(3).
42. Li M, Wang ZW, Fang LJ, Cheng SQ, Wang X, Liu NF. Programmed cell death in atherosclerosis and vascular calcification. Cell Death Dis. 2022;13(5):467.
43. Pang Q, Wang P, Pan Y, Dong X, Zhou T, Song X, Zhang A. Irisin protects against vascular calcification by activating autophagy and inhibiting NLRP3-mediated vascular smooth muscle cell pyroptosis in chronic kidney disease. Cell Death Dis. 2022;13(3):283.
44. Wang Y, Zhang Y, Gao M, Chen Z, Lu J, Li Y, Di Y, Zhao Y, Liu B, Tang R. Lipocalin-2 promotes CKD vascular calcification by aggravating VSMCs ferroptosis through NCOA4/FTH1-mediated ferritinophagy. Cell Death Dis. 2024;15(11):865.
45. Shao S, Liu Y, Hong W, Mo Y, Shu F, Jiang L, Tan N. Influence of FOSL1 Inhibition on vascular calcification and ROS generation through ferroptosis via P53-SLC7A11 axis. Biomedicines, 2023;11(2).

Publisher's note